NANO LETTERS

Letter

pubs.acs.org/NanoLett

Formation of Stable Phosphorus–Carbon Bond for Enhanced Performance in Black Phosphorus Nanoparticle–Graphite Composite Battery Anodes

Jie Sun,[†,#] Guangyuan Zheng,[‡] Hyun-Wook Lee,[†] Nian Liu,[§] Haotian Wang,[∥] Hongbin Yao,[†] Wensheng Yang,*[,#] and Yi Cui*[,†,⊥]

[†]Department of Materials Science and Engineering, [‡]Department of Chemical Engineering, [§]Department of Chemistry, and [∥]Department of Applied Physics, Stanford University, Stanford, California 94305, United States

[⊥]SLAC National Accelerator Laboratory, Stanford Institute for Materials and Energy Sciences, 2575 Sand Hill Road, Menlo Park, California 94025, United States

[#]State Key Laboratory of Chemical Resource Engineering, Beijing University of Chemical Technology, Beijing 100029, People's Republic of China

Supporting Information

ABSTRACT: High specific capacity battery electrode materials have attracted great research attention. Phosphorus as a low-cost abundant material has a high theoretical specific capacity of 2596 mAh/g with most of its capacity at the discharge potential range of 0.4–1.2 V, suitable as anodes. Although numerous research progress have shown other high capacity anodes such as Si, Ge, Sn, and SnO_2, there are only a few studies on phosphorus anodes despite its high theoretical capacity. Successful applications of phosphorus anodes have been impeded by rapid capacity fading, mainly caused by large volume change (around 300%) upon lithiation and thus loss of electrical contact. Using the conducting allotrope of phosphorus, "black phosphorus" as starting materials, here we fabricated composites of black phosphorus nanoparticle-graphite by mechanochemical reaction in a high energy mechanical milling process. This process produces phosphorus–carbon bonds, which are stable during lithium insertion/extraction, maintaining excellent electrical connection between phosphorus and carbon. We demonstrated high initial discharge capacity of 2786 mAh·g^{-1} at 0.2 C and an excellent cycle life of 100 cycles with 80% capacity retention. High specific discharge capacities are maintained at fast C rates (2270, 1750, 1500, and 1240 mAh·g^{-1} at C/5, 1, 2, and 4.5 C, respectively).

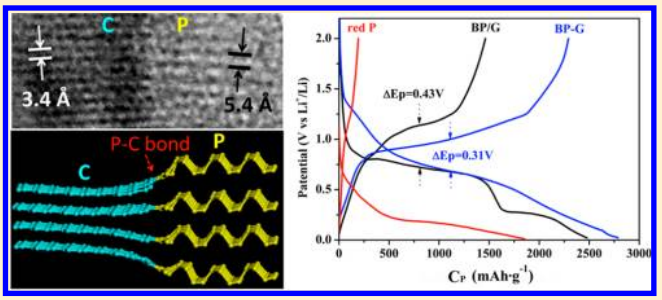

KEYWORDS: *Black phosphorus, carbon, phosphorus–carbon bond, reversible cycle, lithium-ion batteries*

Rechargeable batteries are critical power sources for mobile applications such as portable electronics, electric vehicles, as well as large-scale stationary energy storage.[1−10] Conventional lithium-ion batteries based on graphite anodes and lithium metal oxide cathodes with theoretical specific energy of ~400 Wh/kg and practical specific energy of ~200 Wh/kg cannot satisfy the growing demand for high-energy storage systems. To achieve a quantum leap in the specific energy of lithium-ion batteries, new electrode materials with high specific lithium-storage capacity are required. For high capacity anodes, Si,[10−12] Ge,[13−16] Sn,[17−19] and SnO_2[20] have been studied intensively (Table 1). Particularly, great success has been demonstrated using the approach of nanostructured materials design.[10−20]

Elemental phosphorus (P) is another attractive anode material for lithium-ion[21−27] and sodium-ion[28−30] batteries (Table 1). P can react with three Li or Na atoms to form Li_3P and Na_3P compounds, giving a high theoretical specific capacity of 2596 mAh·g^{-1}. It still has a reasonable anode potential of

Table 1. Specific Capacity and the Potential of Charge and Discharge for Li-Ion Batteries

	specific capacity (m A h g^{-1})	average charge potential (V vs Li$^+$/Li)	average discharge potential (V vs Li$^+$/Li)
graphite	372	0.1	0.17
Si	4200	0.2	0.45
Ge	1600	0.4	0.65
Sn	994	0.4	0.6
P (black)	2596	0.45	0.9

discharge and charge, 0.9 and 0.45 V versus Li metal, 0.65 and 0.3 V versus Na metal, respectively. Despite its slight higher potential compared to other anodes listed in Table 1, P anode

Received: April 30, 2014
Revised: July 2, 2014

   dx.doi.org/10.1021/nl501617j | *Nano Lett.* XXXX, XXX, XXX–XXX

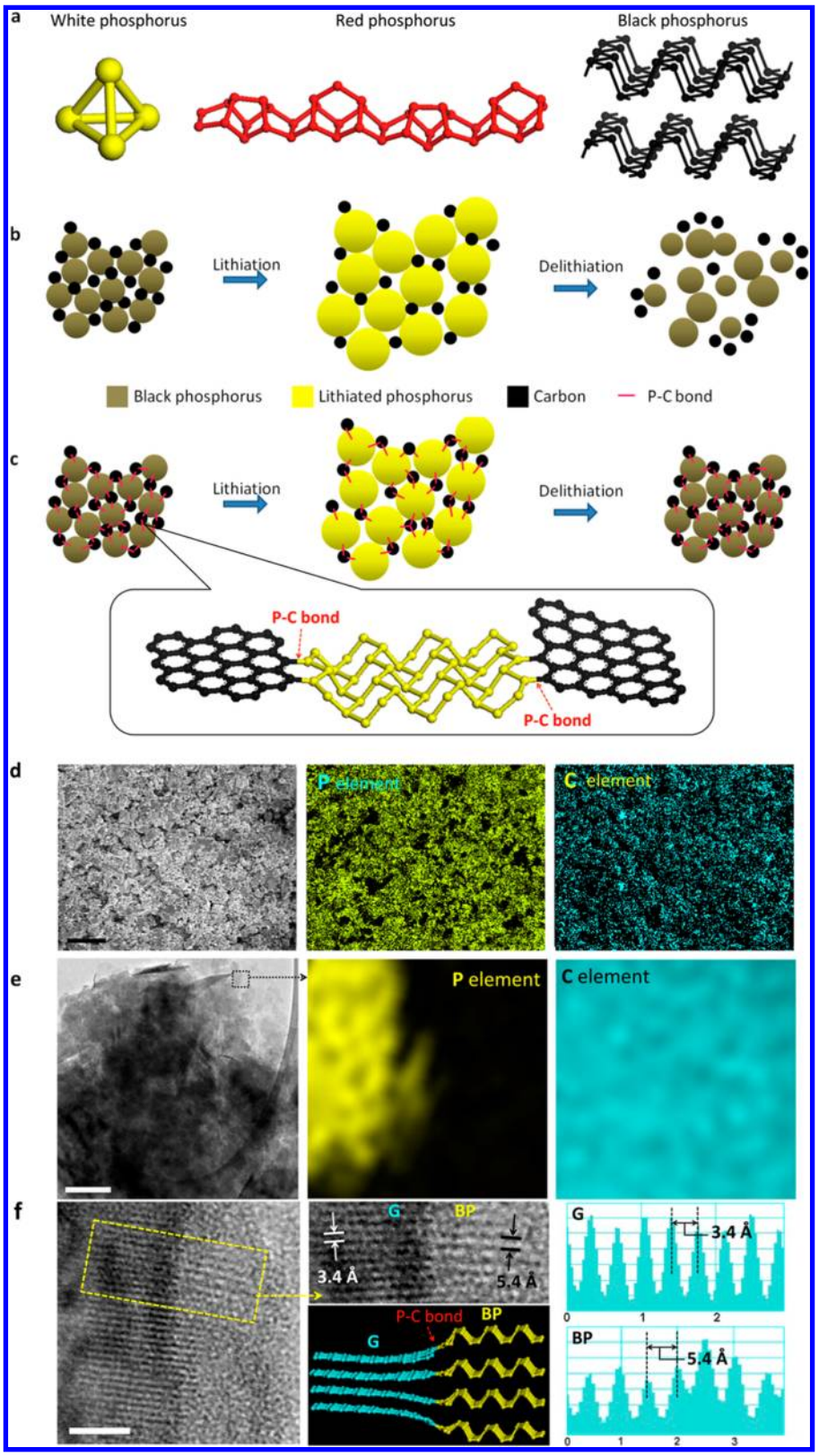

Figure 1. Schematics and characterization of black phosphorus−carbon composite. (a) Schematics of white, red, and black phosphorus. (b) The black phosphorus particles tend to pulverize during cycling because of its large volume expansion. Much of the material loses contact with the carbon conductor, resulting in poor transport of electrons. (c) The stable P−C bond provides a good contact between black phosphorus and carbon conductor even after cycling. (d) FESEM image of the BP-G composite. The corresponding EDS elemental dot-mapping images of C and P elements. Scale bar, 500 nm. (e) TEM image of BP-G composite. The corresponding selected area EELS elemental dot-mapping images of C and P elements. Scale bar, 50 nm. (f) The HRTEM image and schematic of BP-G composite. The corresponding line profiles of the Z-contrast information with the measured spacing between BP and G layers (right). Scale bar, 2 nm.

dx.doi.org/10.1021/nl501617j | *Nano Lett.* XXXX, XXX, XXX−XXX

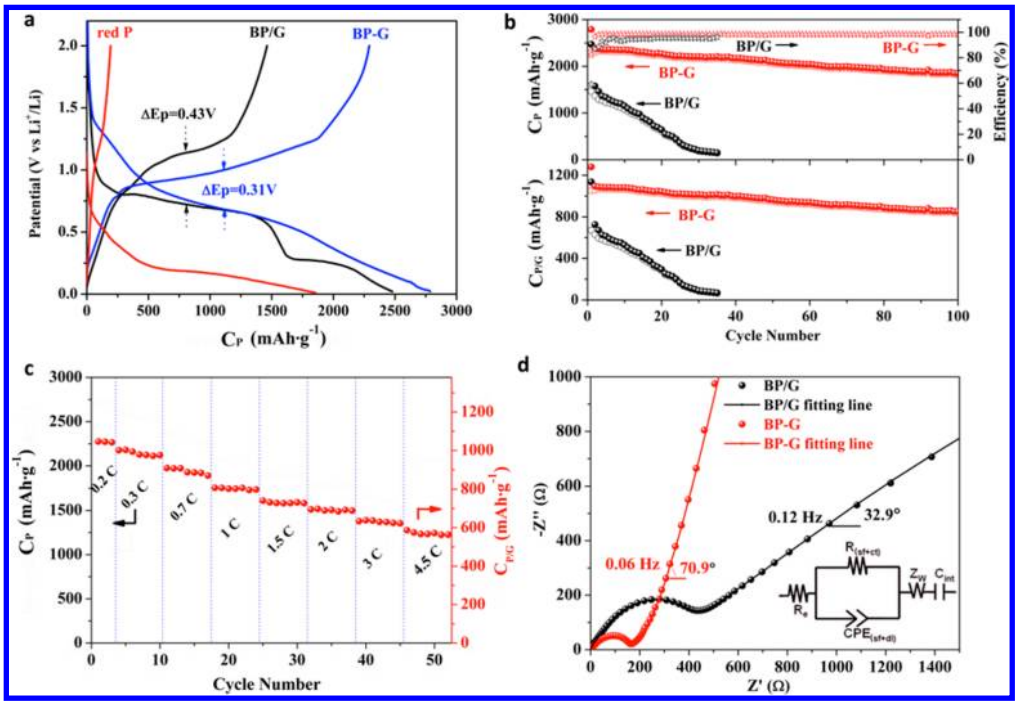

Figure 2. Electrochemical lithium storage performance of the BP-G, BP/G and red P/G electrodes. (a) The charge−discharge profiles of red P, BP/G, and BP-G electrodes at the first cycle between 0.01−2.0 V with a current density of 0.2 C. (b) The cycling performance and Coulombic efficiency of BP/G and BP-G electrodes at a current density of 0.2 C. (c) The rate performance of the BP-G electrode at various current densities from 0.2 to 4.5 C. (d) Nyquist plots and equivalent circuit model of BP/G and BP-G electrodes after 10 cycles at 0.2 C in the discharged state (2.0 V vs Li^+/Li). C_P and $C_{P/G}$ are for the specific capacity calculated based on the weight of BP and BP-G composites, respectively.

can enable high energy batteries. For example, when P anode is paired with Li_2S cathode, the full reaction of $2P + 3Li_2S = 2Li_3P + 3S$ gives an average voltage of ∼1.2 V and a theoretical specific energy of 1207 $Wh·kg^{-1}$, which is about 3 times of that of the graphite/lithium metal oxide batteries. At the same time, the higher lithiation potential of P could be advantageous for fast charging without risking lithium plating.

Solid P has three main allotropes: white,[31] red,[31] and black.[32,33] Among these allotropes, white phosphorus (WP) exists as tetrahedral structured molecules (P_4) (Figure 1a), which is chemically unstable because of large bonding strain. WP begins to burn at 30 °C, so it is not suitable as electrode materials for battery safety. Thus, far red P (RP)[25−30] and black P (BP)[21−24] have been studied as the anode materials because of their chemical stability at room temperature and atmosphere. RP is amorphous (Figure 1a) and thus has low electron conductivity. The orthorhombic BP (layered crystal structure in Figure 1a) is thermodynamically the most stable allotrope, nonflammable and insoluble in most solvents.[21] With its layered structure of puckered sheets and good electrical conductivity, BP is very similar to graphite in terms of appearance, structure, and properties. Indeed, single layer of BP called "phosphorene" can be mechanically exfoliated just like graphene from graphite.[34−36] As shown in Table S2 (Supporting Information), BP has high bulk electrical conductivity (∼10^2 S/m), low band gap (0.34 eV), and reasonable density (2.69 $g·cm^{-3}$), which are beneficial for realizing both high power and energy densities.

The bulk or micron-sized RP has negligible reversible Li-ion storage capacity due to its low electron conductivity.[21] It was found that RP can be transformed into small particles (∼100 nm) of BP using high energy mechanical milling (HEMM) technique, which delivered high first charge and discharge capacities of 2010 and 1814 $mAh·g^{-1}$, respectively.[21] However, the capacity quickly fades only after a few cycles because of the large volume expansion of ∼300% taking place from P to Li_3P (Supporting Information). Similar to the widely studied Si anodes, mechanical fracture induced by large volume change causes the loss of electrical contact of active materials and thus the rapid capacity fade (Figure 1b). In order to improve the capacity retention, Park et al. have controlled the voltage range up to 0.78 V versus Li^+/Li to use the stable reversible reaction of BP.[21] The corresponding reversible reaction between P and LiP provide a reversible specific capacity of only ∼600 $mAh·g^{-1}$. Thus, far, stable rechargeable cycle has not yet been achieved when accessing the full capacity (at least 2000 mAh/g) of black P anodes.[21]

On the basis of our extensive research on the large volume change in Si or Ge anodes[10−13] and the detailed analysis of similar issues in P electrode, we believe that it is critical to maintain good electric connection between P and the conductive carbon matrix during the lithiation process. Here, we demonstrate a strategy for generating robust phosphorus−carbon (P−C) bonds between BP and a variety of carbon materials, including graphite (G), graphite oxide (GO), carbon black (CB), and fullerene (C_{60})). We have achieved significant improvement on the high capacity retention during electrochemical cycling. The XPS and Raman data after electrochemical cycling confirm that the P−C bond is stable during lithium insertion/extraction (Figure 1c), resulting in good electrical contact between BP and C. According to previous reports the P−C bonds in phosphorus carbides could be generated by radio frequency plasma deposition,[37] pulsed laser ablation,[38] and filtered cathodic vacuum arc techniques,[39] while the P-doped graphene with P−C bond was formed via chemical vapor deposition.[40,41] We generated the P−C bonds by

dx.doi.org/10.1021/nl501617j | Nano Lett. XXXX, XXX, XXX−XXX

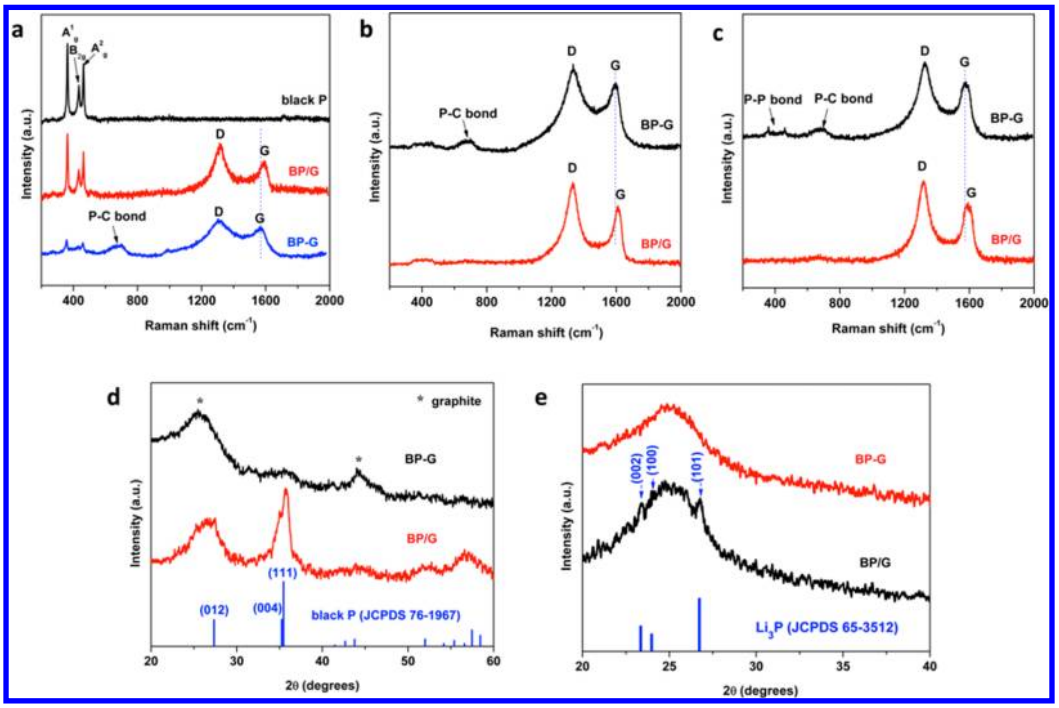

Figure 3. The structural evolution of the BP-G and BP/G undergoing electrochemical processes. (a) Raman spectra of the fresh BP, BP/G, and BP-G with a wavelength of 514 nm as excitation source. (b) Raman spectra of the BP/G and BP-G at the charged state for the first cycle. (c) Raman spectra of the BP/G and BP-G at the discharged state for the 30th cycle. (d) XRD patterns of the BP/G and BP-G. (e) XRD patterns of the BP/G and BP-G in the discharged state (2.0 V vs Li^+/Li) after 30 cycles at a current density of 0.2 A·g^{-1}. The broad peak at around 25° corresponds to graphite.

processing the mixture of BP and carbon materials via HEMM under a 1.2 MPa Ar atmosphere. The impulse of collision during HEMM is about a half of that of a 10 lb. ball bowling at a speed of 10 miles per hour (~20 Huygens), which can generate high energy for a chemical reaction.

Starting from BP-G composite as an example, the average diameter of a particle is around 300 nm, as shown in Figure 1d, which is larger than the raw material of ball-milled BP and graphite (Supporting Information, Figure S1 and S4). The bigger average particle size after the ball-milling is considered by the aggregated secondary particle form of BP and graphite. Interestingly, the secondary particles linked with each other to form a continuous structure, which functions as an electrical pathway and a mechanical backbone so that all nanoparticles are electrochemically active. The energy dispersive spectroscopy (EDS) mapping images reveal uniform distributions of C and P elements in BP-G. In the HRTEM image of one secondary particle in Figure 1e, it is composed of dark and light stacking layers with smaller diameter of about 10 to 50 nm. The dark spot is phosphorus, and the light area is carbon on the basis of the EELS elemental mapping images. The formation of P−C bonds in BP-G is confirmed by the lattice fringes of both BP and G in the HRTEM image. As illustrated in Figure 1f, the cross-sectional HRTEM image of the BP-G shows parallel dark lines with two different spacing. The lattice lines with a smaller spacing of ~0.34 nm correspond to the gap between the two single graphene layer in graphite, whereas the other lines with a larger spacing of ~0.54 nm are assigned as the BP layers. The coherent P−C bonding also is found at the boundary of two different regions. The formation of P−C bond will be further confirmed in detail experiment below.

The formation of coherent P−C bonds in the BP-G composite affords surprisingly high capacity and cycle ability on the battery performance. The electrochemical lithium storage properties of the RP, mixture of BP and graphite (BP/G) without HEMM, and chemically bonded BP-G composite with HEMM were evaluated by galvanostatic charge/discharge measurements as shown in Figure 2a. The C_P and $C_{P/G}$ are reserved for the specific capacity calculated based on the weight of BP and BP-G composites, respectively. The charge and discharge C_P capacity of RP are 1856 and 193 mAh/g, respectively. The charge/discharge profiles of the BP/G mixture at 0.2 C are similar to those of the reported BP.[21−24] When the potential is lowered to 0.78, 0.63, and 0 V from the initial 2 V during the lithiation process, the multistep reaction is ascribed to the conversion of black P → LiP → Li_2P → Li_3P.[21] Although the initial charge C_P capacity of the BP/G electrode was 2479 mAh/g, the first cycle Coulombic efficiency is only 58% caused by the large volume expansion resulting in the lose of electrical contact with G. The BP linked with G (BP-G) via P−C bond, when cycled within the voltage range of 0.01 and 2.0 V, exhibits an initial charge C_P specific capacity of 2786 mAh·g^{-1}. The reversible C_P specific capacity was around 2382 mAh·g^{-1}. Furthermore, the hysteresis (ΔE_p) of the discharge and charge plateaus is reduced from 0.43 to 0.31 V. The reduced ΔE_p offers the evidence that P−C bond improves Coulombic efficiency resulting from the better connection between particles during highly volume changing in lithiation and delithaion processes.

The cycling performance of the BP/G mixture and BP-G composite are compared in Figure 2b. When cycled within the voltage range between 0.01 and 2.0 V, the BP/G mixture showed a much smaller specific capacity. This is caused by the large structural change of the electrode, which results in losing of electrical contact between active material and carbon conductor. The BP-G composite retains a remarkable reversible

dx.doi.org/10.1021/nl501617j | Nano Lett. XXXX, XXX, XXX−XXX

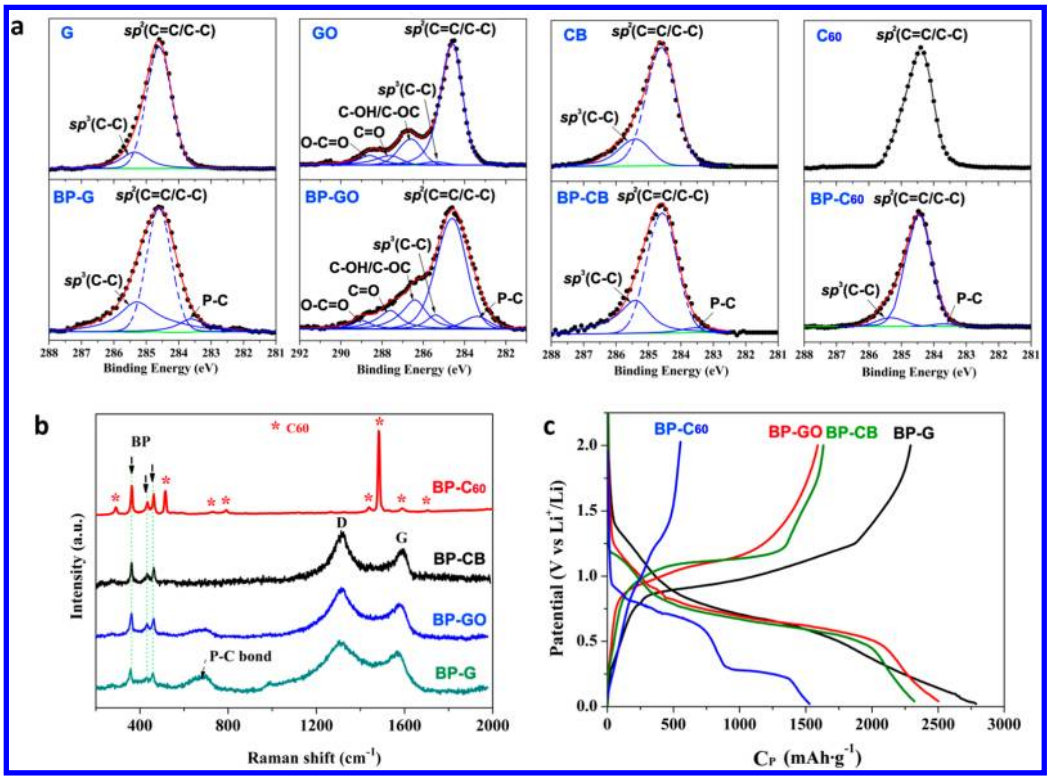

Figure 4. The contribution of different carbon materials for generating the P−C bond. (a) The XPS analysis of the deconvoluted C1s peaks from the various carbon materials and the corresponding black phosphorus (BP)-carbon composites with the results of curve fitting, showing the different chemical states. (b) Raman spectra of the fresh BP-C60, BP-CB, BP-GO, and BP-G with a wavelength of 514 nm as excitation source. (c) The charge−discharge profiles of BP-C60, BP-GO, BP-CB and BP-G electrodes at the first cycle between 0.01−2.0 V with a current density of 0.2 C.

C_P capacity of 1849 mAh·g^{-1} at the end of the 100th cycle. The initial Coulombic efficiency and capacity retention of the BP-G show much better performance and stability than the BP/G using the same BP and G as starting materials. To further test its cycling performance under various high rates, discharge capacities versus cycle number were examined at various current rates from 0.2 to 4.5 C. As shown in Figure 2c, a reversible C_P capacity of 2270 mAh·g^{-1} was realized at 0.2 C. When the current rate was increased to 1 C, the reversible C_P capacity was delivered as 1750 mAh·g^{-1}. Even at higher rates, such as 2, 3, and 4.5 C, the electrode retained a C_P specific capacity of 1500, 1380, and 1240 mAh·g^{-1}, respectively.

To further establish the relationship between electrochemical performance and electrode kinetics for BP-G and BP/G, electrochemical impedance spectroscopy (EIS) was performed. Prior to the EIS tests, the cells were ran for 10 cycles at a current density of 0.2 C to obtain stable electrodes. The tests were then carried out at 2.0 V versus Li$^+$/Li in the discharged state (Figure 2d). The Nyquist plots of the both electrodes consist of a single depressed semicircle in the high-medium frequency region and an inclined line at the low frequency, respectively. The experimental data are represented as symbols (solid circles), and the continuous lines are fitted data according to the equivalent circuit shown in the inset of Figure 2d. The elements in the equivalent circuit include ohmic resistance of the electrolyte and cell components (R_e), surface film resistance (R_{sf}), charge-transfer resistance at the interface between the electrode and electrolyte (R_{ct}), a constant phase element (CPE_i) (surface film (sf), double layer (dl)) used instead of pure capacitance due to the depressed semicircle,[42] Warburg impedance (Z_w), and intercalation capacitance (C_{int}). According to the fitting with this equivalent circuit, the value of R_e is 1.8−2.5 Ω for both samples, indicating that the cells have been properly fabricated and tested in the same condition. Because of the single semicircle observed, the impedance can be ascribed to the combination of the surface film and charge-transfer resistance $R_{(sf+ct)}$. The fitting parameter of $R_{(sf+ct)}$ is much lower for the BP-G electrode (177.4 Ω) compared to the BP/G (484.2 Ω), which means that the BP-G electrode has a more stable surface film (including SEI layer) and faster charge-transfer process than the BP/G electorde. It can be seen that the low-frequency tail for the two samples was also different, which can be compared qualitatively to the mass (mainly of lithium ions) transfer kinetics in the electrode materials. The low-frequency slope angle is 70.9° for BP-G electrode, higher than that of BP/G (32.9°). The steeper low-frequency tail indicates higher lithium ion diffusivity in the electrode materials.[42] As expected, it indicates that the BP-G electrode possesses a high electrical conductivity, a rapid charge-transfer process, and good lithium ion diffusivity for lithium uptake and extraction.

The P−C bonds play a highly important role in the electrochemical performance of the BP-G composite. The structural evolution of the BP-G and BP/G undergoing electrochemical processes have been investigated by Raman and XRD. In Figure 3a, BP, with orthorhombic (A11) phase, has three Raman active modes at 465, 435, and 362 cm^{-1}, which are assigned to A_{2g}, B_{2g}, and A_{1g}, respectively.[43−45] The BP/G mixture retains the Raman active modes of both BP and G. The Raman spectrum of BP-G composite in the region 300−500 cm^{-1} contains bands that are indicative of P−P bonds and shows a significant decrease in intensity because of the

dx.doi.org/10.1021/nl501617j | Nano Lett. XXXX, XXX, XXX−XXX

breakup of some P−P bonds for generating the P−C bonds. A broad envelope centered at ∼700 cm^{-1} in the Raman spectrum of BP-G composite covers the range expected for P−C bond stretching modes (650−770 cm^{-1}), based on theoretical calculations.[38,46] The peaks in the region of 1200−1800 cm^{-1} are the characteristic of graphitic carbon. The G mode of graphite around 1580 cm^{-1} corresponds to the E_{2g} symmetrical bond stretching motion of pairs of C sp^2 atoms, while the D band around 1320 cm^{-1} is attributed to the breathing mode of aromatic rings.[38,46] Comparing with the G band maxima of the BP/G mixture at 1588 cm^{-1}, the BP-G composite has the G band shifted to a lower wavenumber (1569 cm^{-1}) due to the π−p* conjugation, also suggesting the formation of P−C bonds.

In the region between 300 and 500 cm^{-1}, the peaks corresponding to P−P bonds disappeared in both of the BP/G and BP-G at the Li insertion state because of the disruption of P−P bonds to form lithiated phosphorus. The P−C bonds in BP-G composite were maintained (Figure 3b). At the discharge state after 30 cycles (Figure 3c), the BP/G mixture still has no peak at the region 300−500 cm^{-1}, indicating that the P−P bond cannot be rebuilt and lithiation/delithiation process is highly irreversible. In contrast, for the BP-G composite the stable P−C bonds provide a good contact between BP and graphite, so that P−P bonds can be reproduced after 30 cycles (Figure 3c), leading to improved reversibility and prolonged cycling life.

In the XRD pattern (Figure 3d), the diffraction peaks corresponding to both BP and graphite were sustained in the BP/G mixture. However, the characteristic (012), (004), and (111) reflections of orthorhombic BP (JCPDS 76-1967) became weaker in BP-G due to the breakup of some P−P bonds for generation of the P−C bonding. At the discharge state after 30 cycles, the characteristic (002), (100), and (101) reflections of Li_3P (JCPDS 65-3512) can be seen in the BP/G mixture (Figure 3e). Because of the poor conductive Li_3P and the loss of electrical contact with carbon, Li_3P can not be converted to black P at the discharge state.

We have further studied the stability of the different P−C bonding types (sp^3, sp^2 in plane, sp^2 at edge, and sp^2 in aromatic ring) by means of periodic ab initio density functional theory (DFT)[47] calculations. The results illustrate that the shortest length of sp^2 P−C bond in aromatic ring is the most stable because of the π−p* conjugation (Table S3, Supporting Information). In order to further study the contribution of sp^2 and sp^3 bonded carbon atoms for generating the P−C bond, four kinds of carbon materials (C_{60}, CB, GO, and G) with different bonding group were chosen for preparing the BP and carbon composites with the same P/C stoichiometric ratio of 1:3. C_{60} can only produce the sp^2 P−C bond in plane. G can supply sp^2 P−C bond at edge and in aromatic ring, while GO can give all the three kinds of sp^2 P−C bond. The carbon black with low graphitization can provide sp^2 and sp^3 P−C bond.

The four pairs of carbon materials and their corresponding composites were analyzed by XPS spectroscopy to identify the surface chemical composition (Figure 4a). Detailed information about the deconvoluted C 1s peaks is shown in Table S4 (Supporting Information). These assignments agree with previous works.[48−50] C_{60} only has sp^2 bonded carbon atoms. In the corresponding black phosphorus and C_{60} composite (BP−C_{60}), the content of the P−C bond is only 0.8%; meanwhile the sp^3 C−C is present at 285.3 eV and because of that the HEMM breaks the sp^2 C═C/C−C bond and produces defects. In the cases of G, GO, and CB, they have not only sp^2 bonded carbon but also some sp^3 groups. The P−C bonds are present in their relative composites, accompanied by the sp^2 carbon atoms decreasing. Meanwhile, the amount of sp^3 C−C (285.3 eV) increased due to the defects generated from HEMM. The total amount of the other sp^3 groups in GO, including C−OH/C−O−C (287.6 eV), C═O (287.6 eV), and O−C═O (289.0 eV), is approximately constant. BP and G (BP-G) composite has the highest percentage concentration of P−C bonds because graphite can produce the most stable sp^2 P−C bond. As shown in the P2p XPS spectra (Supporting Information, Figure S6), which have been fitted to the $2p^{1/2}$ and $2p^{3/2}$ doublet,[51] the peaks at 130.4 eV ($2p^{3/2}$) and 131.24 eV ($2p^{1/2}$) in the various BP-carbon composites can be assigned to P−C bond.[37−41] The P2p component corresponding to P−C bond has the highest intensity in the BP-G composite, which also indicates that graphite is a good candidate for synthesis of the corresponding BP and carbon composite with P−C bond. As shown in the Raman spectra (Figure 4b), the broad envelope centered at ∼700 cm^{-1} is assigned to P−C bond stretching modes. The intensity of modes in groups BP-G, BP-GO, BP-CB, and BP-C60 were weakened orderly due to the low content of P−C bond. Compared with their galvanostatic discharge−charge curves (Figure 4c), the BP-G have the highest reversible specific capacity.

In summary, we have successfully demonstrated high-performance BP-carbon anodes with formation of stable P−C bonds made from various carbon sources, which act as idea models to systematically study the effects of different carbon sources on the electrochemical properties. Ab initio density functional theory method was carried out to elucidate the chemical interaction between these carbon and BP. Comparing the electrochemical performances of the BP-carbon composites, we found that the carbon structures played essential roles in formation of stable P−C bonds. Among these carbon, graphite was found to be the best choice to enable a long cycle life and high-rate capability, which is attributed to the effective contact between the phosphorus and carbon particles. The present results demonstrate one of the best performances of black phosphorus as an attractive anode material for the next-generation of low-cost, high-capacity lithium ion batteries.

■ ASSOCIATED CONTENT

Supporting Information

Detailed description of the experimental procedures and additional information about material characterization and structural simulation. This material is available free of charge via the Internet at http://pubs.acs.org.

■ AUTHOR INFORMATION

Corresponding Authors

*E-mail: yicui@stanford.edu (Y.C.).
*E-mail: yangws@mail.buct.edu.cn (W.Y.).

Notes

The authors declare no competing financial interest.

■ ACKNOWLEDGMENTS

We acknowledge the support by the U.S. Department of Energy, Office of Basic Energy Sciences, Materials Sciences and Engineering Division, under Contract DE-AC02-76-SFO0515. W.Y. acknowledges support from the National Natural Science Foundation of China under 51272020 and 21236003. H.W.L.

acknowledges support from the Basic Science Research Program through the National Research Foundation of Korea (NRF) funded by the Ministry of Education, Science and Technology under NRF-2012R1A6A3A03038593.

REFERENCES

(1) Goodenough, J. B.; Park, K. S. The Li-ion rechargeable battery: a perspective. *J. Am. Chem. Soc.* **2013**, *135*, 1167−1176.
(2) Mukherjee, R.; Krishnan, R.; Lu, T. M.; Koratkar, N. Nanostructured electrodes for high-power lithium ion batteries. *Nano Energy* **2012**, *1*, 518−533.
(3) Choi, N. S.; et al. Challenges facing lithium batteries and electrical double-layer capacitors. *Angew. Chem., Int. Ed.* **2012**, *51*, 2−33.
(4) Bruce, P. G.; Scrosati, B.; Tarascon, J. M. Nanomaterials for rechargeable lithium batteries. *Angew. Chem., Int. Ed.* **2008**, *47*, 2930−2946.
(5) Li, Y.; Fu, Z. Y.; Su, B. L. Hierarchically structured porous materials for energy conversion and storage. *Adv. Funct. Mater.* **2012**, *22*, 4634−4667.
(6) Wu, X. L.; Guo, Y. G.; Wan, L. J. Rational design of anode materials based on group IVA elements (Si, Ge, and Sn) for lithium-ion batteries. *Chem.—Asian J.* **2013**, *8*, 1948−1958.
(7) Tarascon, J. M.; Armand, M. Issues and challenges facing rechargeable lithium batteries. *Nature* **2001**, *414*, 359−367.
(8) Lu, L.; Han, X.; Li, J.; Hua, J.; Ouyang, M. A review on the key issues for lithium-ion battery management in electric vehicles. *J. Power Sources* **2013**, *226*, 272−288.
(9) Park, C. M.; Kim, J. H.; Kim, H.; Sohn, H. J. Li-alloy based anode materials for Li secondary batteries. *Chem. Soc. Rev.* **2010**, *39*, 3115−3141.
(10) Liu, N.; et al. A pomegranate-inspired nanoscale design for large-volume-change lithium battery anodes. *Nat. Nanotechnol.* **2014**, *9*, 187−192.
(11) Wu, H.; et al. Stable cycling of double-walled silicon nanotube battery anodes through solid−electrolyte interphase control. *Nat. Nanotechnol.* **2012**, *7*, 310−315.
(12) Chan, C. K.; et al. High performance lithium battery anodes using silicon nanowires. *Nat. Nanotechnol.* **2008**, *3*, 31−35.
(13) Chan, C. K.; Zhang, X. F.; Cui, Y. High capacity Li ion battery anodes using Ge nanowires. *Nano Lett.* **2008**, *8*, 307−309.
(14) Rudawski, N. G.; et al. Nanostructured ion beam-modified Ge films for high capacity Li ion battery anodes. *Appl. Phys. Lett.* **2012**, *100*, 083111−1−4.
(15) Song, T.; et al. Si/Ge double-layered nanotube array as a lithium ion battery anode. *ACS Nano* **2012**, *6*, 303−309.
(16) Xue, D. J.; et al. Improving the electrode performance of Ge through Ge@C core−shell nanoparticles and graphene networks. *J. Am. Chem. Soc.* **2012**, *134*, 2512−2515.
(17) Derrien, G.; Hassoun, J.; Panero, S.; Scrosati, B. Nanostructured Sn−C composite as an advanced anode material in high-performance lithium-ion batteries. *Adv. Mater.* **2007**, *19*, 2336−2340.
(18) Qin, J.; et al. Graphene Networks Anchored with Sn@graphene as lithium ion battery anode. *ACS Nano* **2014**, *8*, 1728−1738.
(19) Lee, K. T.; Jung, Y. S.; Oh, S. M. Synthesis of tin-encapsulated spherical hollow carbon for anode material in lithium secondary batteries. *J. Am. Chem. Soc.* **2003**, *125*, 5652−5653.
(20) Kravchyk, K.; et al. Monodisperse and inorganically capped Sn and Sn/SnO_2 nanocrystals for high-performance Li-ion battery anodes. *J. Am. Chem. Soc.* **2013**, *135*, 4199−4202.
(21) Park, C. M.; Sohn, H. J. Black phosphorus and its composite for lithium rechargeable batteries. *Adv. Mater.* **2007**, *19*, 2465−2468.
(22) Nagao, M.; Hayashi, A.; Tatsumisago, M. All-solid-state lithium secondary batteries with high capacity using black phosphorus negative electrode. *J. Power Sources* **2011**, *196*, 6902−6905.
(23) Sun, L. Q.; Li, M. J.; Sun, K.; Yu, S. H.; Wang, R. S.; Xie, H. M. Electrochemical activity of black phosphorus as an anode material for lithium-ion batteries. *J. Phys. Chem. C* **2012**, *116*, 14772−14779.
(24) Stan, M. C.; Zamory, J. V.; Passerini, S.; Nilges, T.; Winter, M. Puzzling out the origin of the electrochemical activity of black P as a negative electrode material for lithium-ion batteries. *J. Mater. Chem. A* **2013**, *1*, 5293−5300.
(25) Wang, L.; et al. Nano-structured phosphorus composite as high-capacity anode materials for lithium batteries. *Angew. Chem., Int. Ed.* **2012**, *51*, 9034−9037.
(26) Marino, C.; Debenedetti, A.; Fraisse, B.; Favier, F.; Monconduit, L. Activated-phosphorus as new electrode material for Li-ion batteries. *Electrochem. Commun.* **2011**, *13*, 346−349.
(27) Qian, J.; Qiao, D.; Ai, X.; Cao, Y.; Yang, H. Reversible 3-Li storage reactions of amorphous phosphorus as high capacity and cycling-stable anodes for Li-ion batteries. *Chem. Commun.* **2012**, *48*, 8931−8933.
(28) Qian, J.; Wu, X.; Cao, Y.; Ai, X.; Yang, H. High capacity and rate capability of amorphous phosphorus for sodium ion batteries. *Angew. Chem. Int. Ed.* **2013**, *125*, 4731−4734.
(29) Kim, Y.; et al. An amorphous red phosphorus/carbon composite as a promising anode material for sodium ion batteries. *Adv. Mater.* **2013**, *25*, 3045−3049.
(30) Li, W. J.; Chou, S. L.; Wang, J. Z.; Liu, H. K.; Dou, S. X. Simply mixed commercial red phosphorus and carbon nanotube composite with exceptionally reversible sodium-ion storage. *Nano Lett.* **2013**, *13*, 5480−5484.
(31) Corbridge, D. E. C. *Phosphorus Chemistry, Biochemistry and Technology*, 6th ed.; CRC Press: Boca Raton, FL, 2013 P1373−1375.
(32) Hultgren, R.; Gingrich, N. S.; Warren, B. E. The atomic distribution in red and black phosphorus and the crystal structure of black phosphorus. *J. Chem. Phys.* **1935**, *3*, 351−355.
(33) Morita, A. Semiconducting black phosphorus. *Appl. Phys. A: Mater. Sci. Process.* **1986**, *39*, 227−242.
(34) Reich, E. S. Phosphorene excites materials scientists. *Nature* **2014**, *506*, 19−19.
(35) Li, L.; et al. Black phosphorus field-effect transistors. *Nat. Nanotechnol.* **2014**, *9*, 372−377.
(36) Liu, H.; Neal, A. T.; Zhu, Z.; Tomanek, D.; Ye, P. D. Phosphorene: An Unexplored 2D Semiconductor with a High Hole Mobility. *ACS Nano* **2014**, *8*, 4033−4041.
(37) Pearce, S. R. J.; May, P. W.; Wild, R. K.; Hallam, K. R.; Heard, P. J. Deposition and properties of amorphous carbon phosphide films. *Diamond Relat. Mater.* **2002**, *11*, 1041−1046.
(38) Fuge, G. M.; May, P. W.; Rosser, K. N.; Pearce, S. R. J.; Ashfold, M. N. R. Laser Raman and X-ray photoelectron spectroscopy of phosphorus containing diamond-like carbon films grown by pulsed laser ablation methods. *Diamond Relat. Mater.* **2004**, *13*, 1442−1448.
(39) Han, J. C.; Liu, A. P.; Zhu, J. Q.; Tan, M. L.; Wu, H. P. Effect of phosphorus content on structural properties of phosphorus incorporated tetrahedral amorphous carbon films. *Appl. Phys. A: Mater. Sci. Process.* **2007**, *88*, 341−345.
(40) Some, S.; et al. Highly air-stable phosphorus-doped n-type graphene field-effect transistors. *Adv. Mater.* **2012**, *24*, 5481−5486.
(41) Zhang, C.; Mahmood, N.; Yin, H.; Liu, F.; Hou, Y. Multifunctional applications for oxygen reduction reaction and lithium ion batteries. *Adv. Mater.* **2013**, *25*, 4932−4937.
(42) Zhou, G.; et al. Oxygen bridges between NiO nanosheets and graphene for improvement of lithium storage. *ACS Nano* **2012**, *6*, 3214−3223.
(43) Akahama, Y.; Kobayashi, M.; Kawamura, H. Raman study of black phosphorus up to 13 GPa. *Solid State Commun.* **1997**, *104*, 311−315.
(44) Vanderborgh, C. A.; Schiferl, D. Raman studies of black phosphorus from 0.25 to 7.7 GPa at 15 K. *Phys. Rev. B* **1989**, *40*, 9595−9599.
(45) Sugai, S.; Shirotani, I. Raman and infrared reflection spectroscopy in black phosphorus. *Solid State Commun.* **1985**, *53*, 753−755.
(46) Claeyssens, F.; Fuge, G. M.; Allan, N. L.; May, P. W.; Ashfold, M. N. R. Phosphorus carbides: theory and experiment. *Dalton Trans.* **2004**, 3085−3092.

dx.doi.org/10.1021/nl501617j | *Nano Lett.* XXXX, XXX, XXX−XXX

(47) Claeyssens, F. Solid phases of phosphorus carbide: An ab initio study. *Phys. Rev. B* **2009**, *79*, 134115−1−14.
(48) Teng, C. C.; et al. Thermal conductivity and structure of non-covalent functionalized graphene/epoxy composites. *Carbon* **2011**, *49*, 5107−5116.
(49) Park, S.; et al. Graphene oxide papers modified by divalent ions-enhancing mechanical properties via chemical cross-linking. *ACS Nano* **2008**, *2*, 572−578.
(50) Park, S.; Ruoff, R. S. Chemical methods for the production of graphene. *Nat. Nanotechnol* **2009**, *4*, 217−224.
(51) Kang, B.; Ceder, G. Battery materials for ultrafast charging and discharging. *Nature* **2009**, *458*, 190−193.

dx.doi.org/10.1021/nl501617j | *Nano Lett.* XXXX, XXX, XXX−XXX